Pergamon

0017–9310(95)00300–2

Experimental and numerical study of buoyancy-induced flow and heat transfer in an open annular cavity

CHETAN P. DESAI and KAMBIZ VAFAI†

Department of Mechanical Engineering, The Ohio State University, Columbus, OH 43210, U.S.A.

Abstract—This paper presents experimental and numerical results for natural convection in a horizontal, annular cavity which communicates with the surroundings through its open end. In the experimental study, a known heat flux was applied to each component of the cavity (inner cylinder, inner cylinder tip, outer cylinder and end-wall) and local surface temperature measurements were made to determine heat transfer characteristics of the convective flow. Trends in the experimental data have been explained in terms of the physical mechanisms underlying the buoyancy induced flow. Smoke flow visualization using laser-induced lighting was performed to understand the flow field around the open end of the cavity. The heat transfer results were correlated by $Nu_{av} = 0.0131(Ra^*)^{0.378}$ for the range of Rayleigh numbers considered ($1.3 \times 10^9 < Ra^* < 5.1 \times 10^9$) in the experiments. In the numerical investigation, solutions to the three-dimensional time-averaged (Reynolds') steady-state equations of fluid motion and heat transfer, were obtained using a finite element analysis. Results of the conjugate study including the local temperature distributions, heat transfer coefficients and the flow field showing the interactions between the ambient and cavity flow fields agreed favorably with experimental results. The present work provides, for the first time, validated heat transfer data for high Rayleigh number buoyancy-induced flows in open annular cavities. Copyright © 1996 Elsevier Science Ltd.

1. INTRODUCTION

The study of free convection in open-ended structures has received a great impetus in recent years because several applications of practical interest can be modeled around the basic geometry associated with it. Fire research, passive solar heating, energy conservation in buildings, cooling of electronic components, cooling of aircraft brakes are some of the areas in which these studies could serve as valuable design aids. One of the main characteristics of buoyancy induced flows in open-ended structures is its basic geometry which, among other aspects, reveals the interactions and the influence of the inner (inside the cavity) and outer (the open region) flow and temperature fields. A limited amount of work has been done in the past to understand such interactions. In addition to constituting a fundamental area of research in heat transfer, understanding these interactions allows a better identification of the design parameters in a number of practical applications.

A theoretical analysis of open cavity problems poses the inherent challenge of specifying boundary conditions at the open end. Most numerical studies on two-dimensional rectangular open cavities have utilized the standard (and more viable) approach of performing calculations in a computational domain extended beyond the cavity and applying the far field

conditions at the boundaries of the extended domain [1–6]. It has been shown by Vafai and Ettefagh [5, 6] that the extent of the enlarged computational domain has a more pronounced effect on the results than those anticipated by previous researchers. A limited number of experimental studies of natural convection in open rectangular cavities have been reported, mainly due to the additional complications of controlling the ambient conditions. The experimental investigation of Bejan and Kimura [7] served to validate their theoretical study of free convection penetration into a rectangular cavity. It was shown that the flow consists of a horizontal counterflow which penetrates the cavity over a distinct length. Further insight into two-dimensional rectangular open cavity natural convection was provided by the experimental studies of Sernas and Kyriakides [8], Hess and Henze [9], and Chan and Tien [10].

While two-dimensional natural convection in open rectangular cavities has been studied to some extent, the more complex, three-dimensional phenomenon of natural convection in open annular cavities has been the subject of attention very recently. A numerical solution to this problem was first obtained by Vafai and Ettefagh [11]. In their study, the inner cylinder was maintained at a constant higher temperature while the outer cylinder was maintained at the lower ambient temperature. The three-dimensional transient laminar analysis performed in an extended computational domain illustrated the effect of axial con-

---

† Author to whom correspondence should be addressed.

NOMENCLATURE

A	exposed surface area of component under consideration	R_c	radius of the extended computational domain
A_h	surface area of the heater on a particular component	r	radial coordinate
dA	elemental surface area	T	temperature
g	gravitational acceleration	T_m	average cavity temperature
h	heat transfer coefficient	T_{χ}	ambient temperature
h_m	average heat transfer coefficient	t	thickness of the cavity components
k	turbulent kinetic energy	U	characteristic velocity of the natural convection flow
L	length of the open annular cavity	u	velocity
L_e	length of the extended computational domain	u_r	radial velocity
		u_θ	azimuthal velocity
Nu	Nusselt number $= hR_o/\lambda$	u_z	axial velocity
Pr	Prandtl number $= v/\alpha$	x	Cartesian coordinate
p	pressure	z	axial location.
Q	total power supplied to the heaters		
Q_{loss}	heat loss from the insulation and radiation heat loss from the test section	**Greek symbols**	
q	applied heat flux	α	thermal diffusivity
q_c	convected heat flux	β	volume expansion coefficient
Ra	Rayleigh number $=$	ε	dissipation of turbulent K.E.
	$g\beta(T_m - T_{\chi})R_o^3/\alpha v$	v	kinematic viscosity
Ra^*	modified Rayleigh number $=$	μ	dynamic viscosity
	$g\beta q R_o^4/\lambda\alpha v$	λ	thermal conductivity
R_i	outer radius of the inner cylinder	θ	angular location measured from the top.
R_o	inner radius of the outer cylinder		

vection on the flow and temperature fields inside the cavity. The recirculating nature of the classical annular natural convection flow coupled with the strong axial convection effects induced by the open end elucidated several fundamental aspects of the flow field. Desai and Vafai [12] reported results from a laminar three-dimensional analysis for natural convection cooling of an open ended annular cavity. Numerical results were obtained for $Ra = 10^4$ and 10^6 and it was discovered that, at the higher Rayleigh numbers, there exist two spirally rotating cells inside the cavity, separated by an axially stagnant flow region. Reducing the inner cylinder length pushed this stagnant zone away from the open end, resulting in higher heat transfer rates due to increased interaction of ambient fluid with the cavity fluid.

High Rayleigh number natural convection in open annular cavities has not been studied to date. In the present work, results from a combined experimental and numerical study of natural convection flow and heat transfer around an open annular cavity are discussed. Experiments were performed and heat transfer correlations obtained for the annular cavity over a wide range of heating conditions. In a concurrent numerical study, a finite element model of the open annular cavity was developed to simulate conditions in the experimental investigation. The numerical and experimental results are shown to be in excellent

agreement. An additional purpose of this investigation was to obtain validated heat transfer data and improved physical understanding of fundamental aspects of natural convection in open annular cavities.

2. EXPERIMENTS

2.1. Experimental apparatus and procedure

A schematic sketch of the test section and its components is shown in Fig. 1. The test section is an open annular cavity bounded by the inner cylinder, outer cylinder and end-wall. High conductivity aluminum alloy (6061-T6) was utilized for fabricating the heated portion of the test-section assembly. The thickness of each cavity component was 6.35 mm. A tube of 508 mm i.d. and 88.9 mm length constituted the outer cylinder while the inner cylinder had an o.d. of 190.5 mm and 82.55 mm length. The inner cylinder tip facing the ambient air had a 190.5 mm dia. The end-wall was machined into an annular plate 520.7 mm o.d. × 177.8 mm i.d. These components were assembled to obtain the open annular cavity for testing purposes. The experimental errors were minimized by using high conductivity screw fasteners and high conductivity paste during assembly. Adequate insulation was provided at the points of contact between the main holding frame and the test section to minimize heat loss by conduction through the frame. Concentric rings
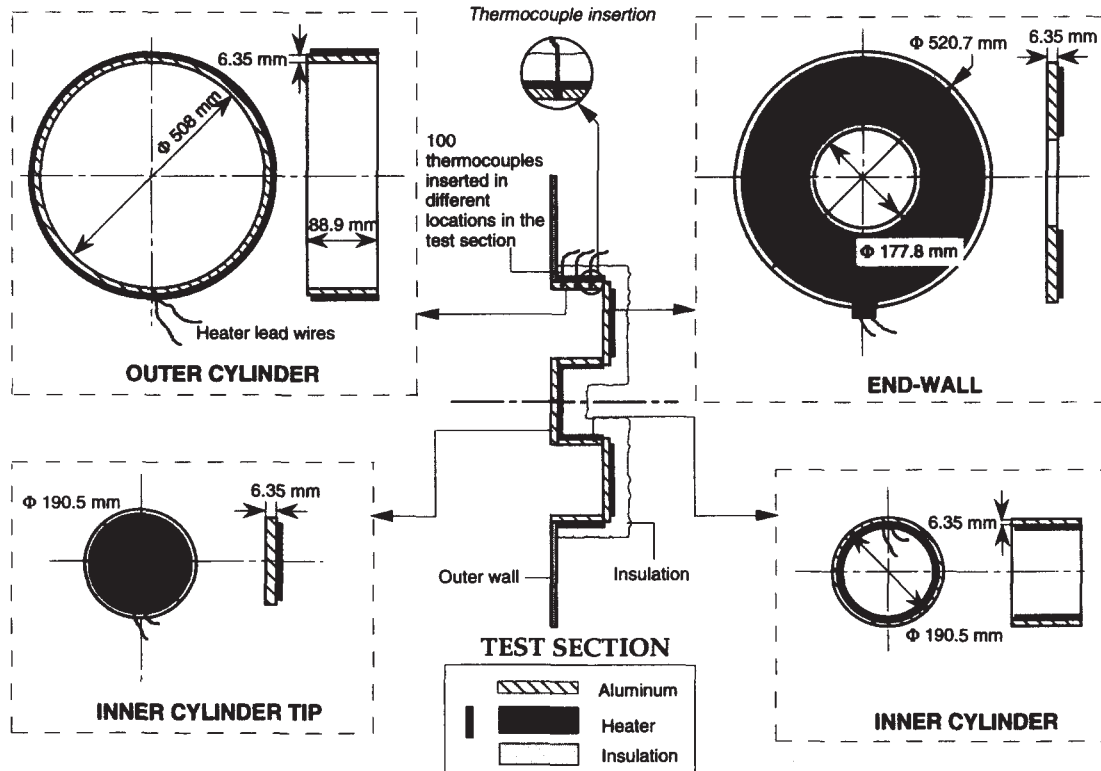
Fig. 1. Test section components used in the experimental study.

(6.35 mm in thickness) of masonite wood and lexan were joined together to construct the outer insulated wall of the test-section. The inner ring was made of masonite wood which was capable of withstanding the high temperatures attained during the experiments. The i.d. of the masonite ring was equal to the o.d. of the outer cylinder and it was mounted flush on the outer cylinder. The wooden ring was then attached to a larger lexan ring to increase the o.d. of the outer wall to 1143 mm. The outer wall was secured in position by four springs attached to the main holding frame of the assembly. The assembled components were then mounted on a base to allow easy movement and change of orientation of the test-section.

The cavity was heated by applying a constant heat flux to each of the cavity components. Flexible silicon rubber thermofoil heaters were attached to the aluminum components by means of a high conductivity pressure sensitive adhesive (PSA) to provide enhanced thermal contact. The heaters were capable of raising the temperature of the test-section up to 260°C. The backside of the heaters was covered with Fiberfrax Durablanket S insulation (thermal conductivity = 0.029 W m^{-1} K^{-1}) to minimize heat losses. For thermocouple insertion, 3 mm dia. holes were drilled through the heaters and corresponding locations in the test-section components. In the test-section, these thermocouple wells were drilled to a depth of 6.2 mm measured from the heater side. Each well was com-

pletely filled with OMEGA high thermal conductivity cement to minimize the effects of removing the material from the test section. The thermocouples (30-AWG K-type) were secured in place inside these wells by the high conductivity cement, taking care to ensure that the tip of the thermocouple was in contact with the bottom of the well. Since the well was drilled to within 0.15 mm of the surface of the aluminum parts in contact with the circulating air, it can be assumed that the thermocouple output was indeed the temperature of the surface in contact with the surrounding air. To determine the heat loss through the insulation, the temperature drop across the insulation on the backside of the heaters was recorded by two thermocouples. The temperature of the ambient air was also measured continuously by a thermocouple placed at an adequate distance away from the test-section.

The heaters were connected to a d.c. power supply (Sorensen DCR 300) capable of providing up to 10 kW. The voltage and current through the heaters was measured by a voltmeter and ammeter built in with the power supply. The temperature data was recorded by a data acquisition unit (HP3497A) and a high accuracy digital voltmeter (HP3458). The heating and data acquisition procedures were fully automated. The experimental set-up including the instrumentation used is depicted in Fig. 2. The experiments were carried out in an isolated room with precise control over the air circulation. The air supply to the
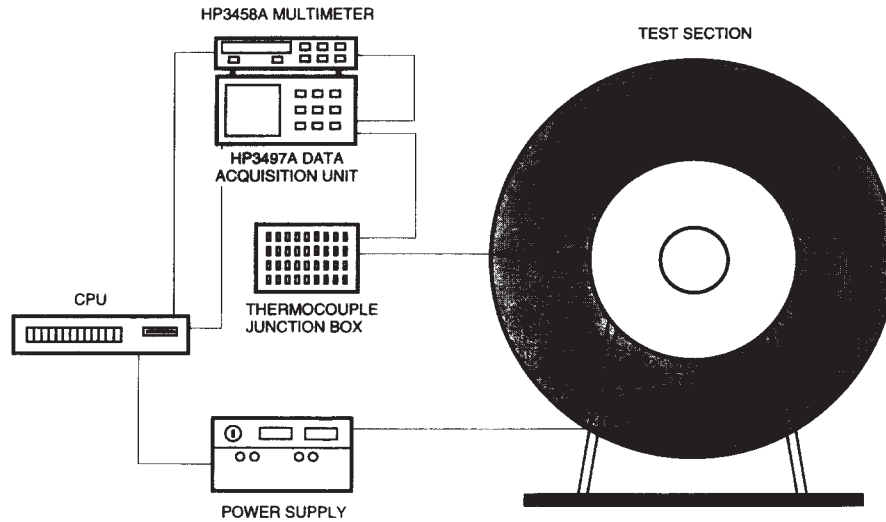
Fig. 2. Schematic layout of experimental set-up and instrumentation.

room was completely shut off at least an hour prior to the start of each experimental run. The thermocouple readings were scanned by the data acquisition unit while the DVM measured the thermocouple output (in volts) for each channel. The temperature values were written to disk before beginning the next scan. Data was collected until steady state, which was satisfied as follows. First, the experiment was allowed to run for at least 5 h. Then, steady-state conditions were assumed to have been reached when the temperature variations were no more than $\pm 0.1^\circ$C for a time span of at least 30 min. Duplicate experimental runs carried out at each Rayleigh number showed results to be repeatable within $\pm 1^\circ$C and even these differences were mainly due to the change in ambient temperature. At the end of each experimental run, the heater power and temperature data was stored for subsequent data reduction and analysis.

Flow visualization studies were made to gain a qualitative understanding of the flow patterns near the open end of the cavity. A Nd : Yag laser with a frequency doubling crystal provided the light source for these experiments, giving a well-collimated beam of green light (wavelength = 532 nm). A lens and mirror assembly, mounted on high precision optical tables, expanded the light beam into two orthogonal sheets, one parallel to the radial (r–θ) plane and the other parallel to the axial (r–z) plane of the cavity. The generation of light sheets and their motion using a stepper motor driven traversing mechanism, was fully automated and controlled by the CPU. Incense sticks were ignited in two separate plexiglas chambers, to generate a large quantity of seeding particles for flow visualization. The smoke from these chambers was then led to a plexiglas stagnation chamber through four PVC pipes, each approximately 90 cm long, to ensure that the seeding particles were neutrally buoyant. The stagnation chamber which had a lid at its top was placed near the test section. When

sufficient amount of smoke was accumulated in the stagnation chamber, the lid was gradually opened so that the seeding particles entered the natural convection flow field. Images of the flow field were then recorded by a CCD camera and stored for image processing.

2.2. Data reduction and uncertainty analysis

An average heat transfer coefficient for each cavity component and also for the entire cavity was defined as

$$h_{\mathrm{m}} = \frac{q_{\mathrm{c}}}{(T_{\mathrm{m}} - T_{\chi,)}}, \tag{1}$$

where q_{c}, the convected heat flux, is calculated using

$$q_{\mathrm{c}} = \frac{q A_{\mathrm{h}}}{A} = \frac{Q - Q_{\mathrm{loss}}}{A}. \tag{2}$$

In the above expression, Q is the total heat input from the power supply, Q_{loss} includes the radiation heat loss from the test section as well as heat loss from the backside of the heaters (through the insulation), A_{h} is the heater area, A is the exposed area and q is the effective input heat flux. The mean temperature (T_{m}) is a weighted area average given by

$$T_{\mathrm{m}} = \frac{\displaystyle\int T \, \mathrm{d}A}{\displaystyle\int \mathrm{d}A}. \tag{3}$$

The Nusselt number and modified Rayleigh number are defined as

$$Nu = \frac{h R_{\mathrm{o}}}{\lambda} \tag{4}$$

$$Ra^* = \frac{g \beta q R_{\mathrm{o}}^4}{\lambda \alpha \upsilon}. \tag{5}$$

The thermophysical properties of air were evaluated at the film temperature, which is defined as the average of the mean cavity surface temperature (T_m) and the temperature of the ambient air (T_∞).

The uncertainty associated with the length scale (R_o) used in the data reduction procedure was ± 0.1 mm. The accuracy in the temperature measurements based on in-house calibration of the thermocouples against a standard thermometer, showed temperature measurement capabilities within $\pm 0.2°C$. The thermocouple outputs were measured within ± 0.01 μV, corresponding to a sensitivity of $2.5 \times 10^{-4}°C$. The uncertainties in the measurement of the heater current and voltage were $\pm 1.5\%$. The uncertainty in the applied heat flux was estimated between 4 and 6%. The thermophysical properties of air were assigned an uncertainty of $\pm 3.0\%$, based on the observed variations in the reported values in the literature. The uncertainties in the Nusselt number and modified Rayleigh number were calculated by the method described by Kline and McClintock [13] and Moffat [14]. The uncertainty in the Nusselt number obtained from the experiments is calculated to lie between 5.1 and 7.2%, whereas that in the modified Rayleigh number was between 7.9 and 9.1%.

3. NUMERICAL STUDY

The physical model and coordinate system for the open annular cavity under consideration are illustrated in Fig. 3. The thermophysical properties of the walls and the working fluid, i.e. air, were assumed to be independent of temperature. Air was assumed to be Newtonian, incompressible and the Boussinesq approximation was invoked. The governing equations are the Reynolds' time-averaged equations of fluid motion coupled with the energy equation in the fluid and in the solid walls of the computational domain. The k–ε model was used to simulate turbulent characteristics of the convective flow.

The application of the turbulence modeling approach used in the present work to complicated forced flows involving strong and subtle flow reversal has already been demonstrated by Haroutunian and Engelman [15]. This model was found to be more accurate and computationally more effective than the k–ε model using standard wall functions. In this approach, the elliptic form of the mean conservation equations (conservation of mass, momentum and energy) was solved throughout the computational domain. The viscosity-affected region between the wall and the fully turbulent region away from the wall was connected by means of a single layer of special elements. These specialized shape functions which were based on universal near-wall profiles accurately resolved the velocity and temperature profiles near the wall.

It was assumed that no exchange of energy occurs across the vertical symmetry plane of the annular cavity. This fact was also confirmed by the experimental results. Therefore, the boundary conditions at this symmetry plane are:

$$u_\theta = 0, \quad \frac{\partial u_r}{\partial \theta} = \frac{\partial u_z}{\partial \theta} = \frac{\partial T}{\partial \theta} = \frac{\partial k}{\partial \theta} = \frac{\partial \varepsilon}{\partial \theta} = 0$$

$$\text{at} \quad \theta = 0, \pi. \quad (6)$$

The no-slip boundary condition for velocity was applied at all the solid walls of the computational
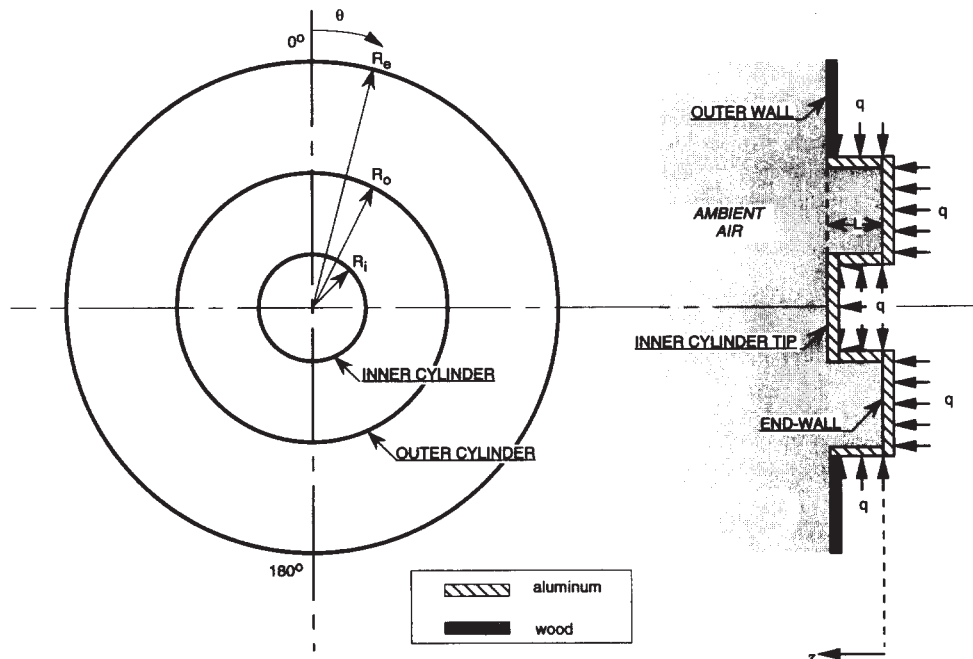

Fig. 3. Physical model and computational domain for the open annular cavity test section.

domain. Further details of the turbulence model can be found in our earlier paper [16] and have not been presented here for brevity.

At the aperture plane, where fluid enters and leaves the cavity, prescribing the boundary conditions requires special care. Two alternate approaches can be used:

(i) imposing boundary conditions at the aperture plane itself;

(ii) applying the far-field conditions at the boundaries of an extended computational domain.

Chan and Tien [17] showed that the simplified approach (i) can provide fairly accurate mean heat transfer results. However, this approach does not account for the corner and outer region. The second approach, on the other hand, has the advantage of including the aperture plane in the computations and therefore provides more realistic results, especially near the cavity opening. In the present work, the second approach was adopted and numerical calculations were performed in a computational domain extended beyond the open end. The extension to the computational domain is basically a cylinder of radius R_c and length L_c, as shown in Fig. 3.

Different far-field boundary conditions were examined for obtaining a realistic set which rendered accurate solutions. After extensive numerical experimentation, the most appropriate set of far-field boundary conditions was obtained (based on an earlier study by Desai and Vafai [12]). The zero gradient of temperature was imposed at the radial boundary of the computational domain while applying a constant ambient temperature at the axial end of the computational domain. This is expressed as

$$\frac{\partial T}{\partial r} = 0 \quad \text{at} \quad r = R_c \quad \text{and} \quad T = 0 \quad \text{at} \quad z = L + L_c.$$

(7)

Based on further numerical experimentation, it was determined that the following boundary conditions on velocity resulted in the most realistic simulation of far field conditions.

$$u_z = 0, \quad \frac{\partial u_r}{\partial r} = \frac{\partial u_\theta}{\partial r} = 0 \quad \text{at} \quad r = R_c$$

$$\text{and} \quad u_r = u_\theta = 0, \quad \frac{\partial u_z}{\partial z} = 0 \quad \text{at} \quad z = L_c. \quad (8)$$

For kinetic energy and dissipation, zero normal gradient was imposed on both the radial as well as axial boundaries of the domain:

$$\frac{\partial k}{\partial r} = 0 \quad \frac{\partial \varepsilon}{\partial r} = 0 \quad \text{at} \quad r = R_c$$

$$\text{and} \quad \frac{\partial k}{\partial z} = 0 \quad \frac{\partial \varepsilon}{\partial r} = 0 \quad \text{at} \quad z = L_c. \quad (9)$$

Dimensions of the extended computational domain

were obtained by rigorous numerical experimentation. Calculations were first made using an extended computational domain equal to three times the size of the cavity. Maintaining the same grid configuration up to three times the cavity size, the domain extension was then increased to six times the cavity size and results were obtained. Comparison showed that results differed by less than 1% in regions close to the cavity (for distances up to 1.5 times the cavity size). The procedure was repeated with a finer grid and the same observations were made. Next, the extension was reduced to twice the cavity size. This time, the results changed by as much as 5% when compared against the results obtained above. Hence, in the present work, all calculations have been performed with an extended computational domain of size equal to three times the cavity size.

Finally, the interfacial boundary conditions between the cavity walls and air, the outer wall and air and also the outer cylinder and outer wall were satisfied. The discretization of the set of governing equations along with boundary conditions was accomplished by using a finite element formulation based on the Galerkin method of weighted residuals (FIDAP [18]). The discretization procedure yielded a system of highly coupled and non-linear algebraic equations. These equations were solved by using an iterative solution scheme based on the segregated solution algorithm which involves decomposition of the entire system of equations into smaller subsystems corresponding to each independent variable. Each subsystem was then solved by using an iterative solver based on a combination of the conjugate residual and conjugate gradient schemes. Convergence was assumed when the relative change in variables between consecutive iterations was less than 0.1%.

4. RESULTS AND DISCUSSION

The annular cavity had a radius ratio (R_i/R_o) of 0.375, length to outer cylinder radius ratio (L/R_o) of 0.35 and a wall thickness to outer cylinder radius ratio (t/R_o) of 0.025. Several experiments were performed for the test-section at different levels of power input which produced average cavity temperatures ranging from 49 to 132°C. During the experimental runs, the ambient air temperature was between 22 and 23°C. The experiments thus covered a modified Rayleigh number of $Ra^* = 1.3 \times 10^9 – 5.1 \times 10^9$.

Numerical results corresponding to some of the experimental runs were obtained using the finite element analysis described in the previous section. Various combinations of grid size were tested to ensure that the results were invariant with respect to the grid size. A systematic grid refinement procedure was adopted and is briefly mentioned here. Initially, the grid-size in the axial direction was held constant. The number of grid points in the radial direction was increased successively with a fixed number of points in the angular direction. Next, the mesh was refined

in the angular direction by using the grid size in the radial direction obtained from the previous step. The number of points required in the radial plane of the cavity was thus established. The number of points in the axial direction was then varied. Finally, the number of grid points in all three directions was increased from the above values to determine the grid size required to obtain a grid-dependent solution.

Within the cavity, 41 points in the radial direction, 45 points in the angular direction and 27 points in the axial direction were required to obtain grid-independent results for the range of Rayleigh numbers considered. A minimum of three grid points were always used in the solid wall thickness of the computational domain. Further, in the fluid region, a variable mesh strategy was adopted. The mesh was always finer near the walls (typically the mesh size near the walls was one half the size of the mesh in the interior of the domain). In the domain extension beyond the open end of the annular cavity, the maximum mesh size (i.e. the mesh size at the far-field locations) was of the order of 10 times the mesh size inside the cavity. For all computational runs, approximately 100 000 elements were required to obtain grid-independent results.

The turbulence modeling approach was rigorously checked by focusing on turbulent buoyancy-driven flow in an annulus bounded by concentric, horizontal cylinders and adiabatic end walls using both two-dimensional and three-dimensional analyses. Results were obtained for Rayleigh numbers ranging from 10^6 to 10^9 and the effects of Prandtl number and radius ratio on the flow and heat transfer characteristics were examined [16]. Good agreement was obtained between the results from this investigation and previous works [19, 20]. Comparison of results from the three-dimensional model with experimental results of McLeod and Bishop [21] showed good agreement. Furthermore, to establish the two-dimensionality of the flow field in the core region of the annulus, the velocity profiles and temperature distributions obtained from the two models were compared and found to be in excellent agreement with each other.

4.1. Flow field

The flow field in each radial plane of the annular cavity is exemplified by the velocity distribution in the mid-axial location shown in Fig. 4a. The velocity magnitudes were non-dimensionalized with respect to the characteristic velocity

$$\left(U = \frac{\alpha}{R_o} \sqrt{Ra^* Pr} \right)$$

used to non-dimensionalize the governing equations. The radius of the outer cylinder (R_o) was chosen as the reference length in all the figures. The peak velocities occur close to the outer cylinder and inner cylinder, indicating the sharp velocity gradients in the turbulent regime. The core flow has low velocities and is driven

by the upward flows along the inner cylinder, outer cylinder and end-wall. Boundary layer separation occurs near the top of the inner cylinder which results in a buoyant plume rising toward the outer cylinder. After impinging on the outer cylinder, part of this flow turns and encounters the upward counterflow along the outer cylinder. The interaction of these flows leads to the formation of a mixing zone near the outer cylinder at approximately 5–10° from the top angular position. The location of this point is dictated by the relative strengths of the buoyant plume from the inner cylinder and the flow along the outer cylinder. The velocity distribution in the symmetry plane (Fig. 4b) shows the axial inflow into the open annular cavity through the lower region. Furthermore, the exiting flow velocity is much higher than the velocity of the incoming fluid.

The flow pattern in each radial plane of the cavity remains essentially similar to the flow field in the mid-axial plane explained above. The axial velocities in four planes of the cavity located one-quarter of the length apart, including the aperture plane of the cavity, are depicted by means of "surface" plots in Fig. 5. In this figure, the zero axial velocity is identified by the solid walls of the cavity. The values above this reference plane indicate positive axial velocities (flow away from the end-wall, i.e. toward the open end) while values below the reference plane indicate negative axial velocities (flow toward the end-wall, i.e. into the cavity). As mentioned earlier, the entry of fluid into the cavity is mainly through the lower half of the cavity. However, fluid influx is also observed in regions around the upper portions of the inner cylinder. Fluid flow toward the open end is stronger in the upper half of the cavity and is maximum at the topmost location. The slight decrease in axial velocity (about 5–10°) from the top is due to the impingement of the inner cylinder plume on the outer cylinder. The outflow velocities (positive component) increase steadily toward the open end, indicating the influence of the outer flow field conditions. The considerable increase in the axial velocity in the exit plane is also obvious from Fig. 6d. There is also an outflow of fluid through small regions below the inner cylinder.

Figure 6 shows the fluid particle paths obtained from the numerical results for $Ra^* = 3.71 \times 10^9$. These pathlines basically show the trajectories of massless fluid particles injected into the flow field just outside the cavity at $z = 0.425$. The particles were assumed to be introduced in the flow field at angular locations 30° apart at $r = 0.1$ to 1.1 ($\Delta r = 0.1$). Based on these particle path plots and many other numerical and flow visualization experiments, the flow structure within the annular cavity in the turbulent regime can be classified as follows. The suction mechanism yields an axial inflow of ambient fluid into the lower half of the cavity in the symmetry plane. Part of this incoming fluid gets entrained into the boundary layers along the inner and outer cylinders while the remaining fluid proceeds along the axial direction toward the end-
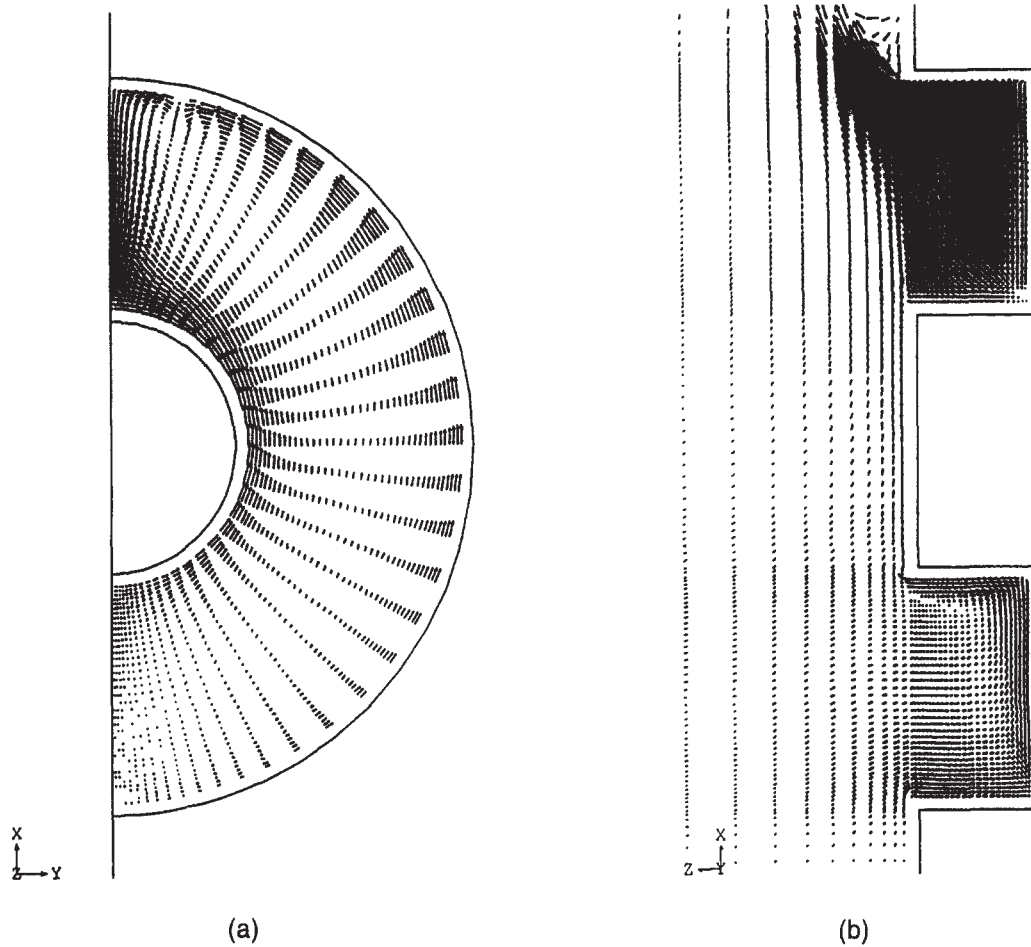
(a)   (b)

Fig. 4. Velocity vector field in the cavity; $Ra^* = 3.71 \times 10^9$, (a) $z = L/2$ (mid-axial plane), (b) vertical symmetry plane.

wall. Some of the fluid particles that penetrate the cavity completely rise in a boundary layer along the end-wall. The presence of the solid-wall induces the fluid recirculation just below the inner cylinder. Fluid motion in the upper half of the symmetry plane is primarily characterized by the rising plume from the top of the inner cylinder and a strong axial outflow of the heated fluid. The "ejection" of fluid as a buoyant jet from the top of the cavity is one of the distinct characteristics of open cavity flows. At the aperture plane, there is an outflow just below the inner cylinder and an inflow just above it. An upward flow along the inner cylinder tip can also be observed. Part of this flow gets entrained into the cavity due to the local suction effect at the top of the inner cylinder while the remaining portion is entrained within the buoyant plume rising from the inner cylinder at the aperture plane.

Pertinent qualitative features of the flow were also observed through the flow visualization experiments. The presence of the strong buoyant outflow near the top of the annular cavity could be observed in the experimental investigation. The local inflow through

regions above the inner cylinder could also be observed. Generally, the experimental studies showed the smaller velocities in the lower regions of the cavity while the velocities were significantly higher in the upper region of the cavity. Hence, the area occupied by the exiting flow was found by both the numerical and flow visualization experiments to be significantly smaller than that occupied by the flow entering the cavity.

4.2. *Heat transfer results*

In the experimental investigation, 100 thermocouples were used to determine the temperature distribution over the surface of the test section. For the inner cylinder, temperatures at 10 different angular positions were recorded in three radial planes of the cavity at $z = 0.05$, 0.15 and 0.25. For the outer cylinder, the planes of interest were located at $z = 0.08$, 0.16 and 0.24 with 10 thermocouples in the angular direction in each plane. For the end-wall, temperatures were measured at nine positions $40°$ apart and at radii $r = 0.53$, 0.69 and 0.85, respectively. The above radial and axial coordinates have been non-
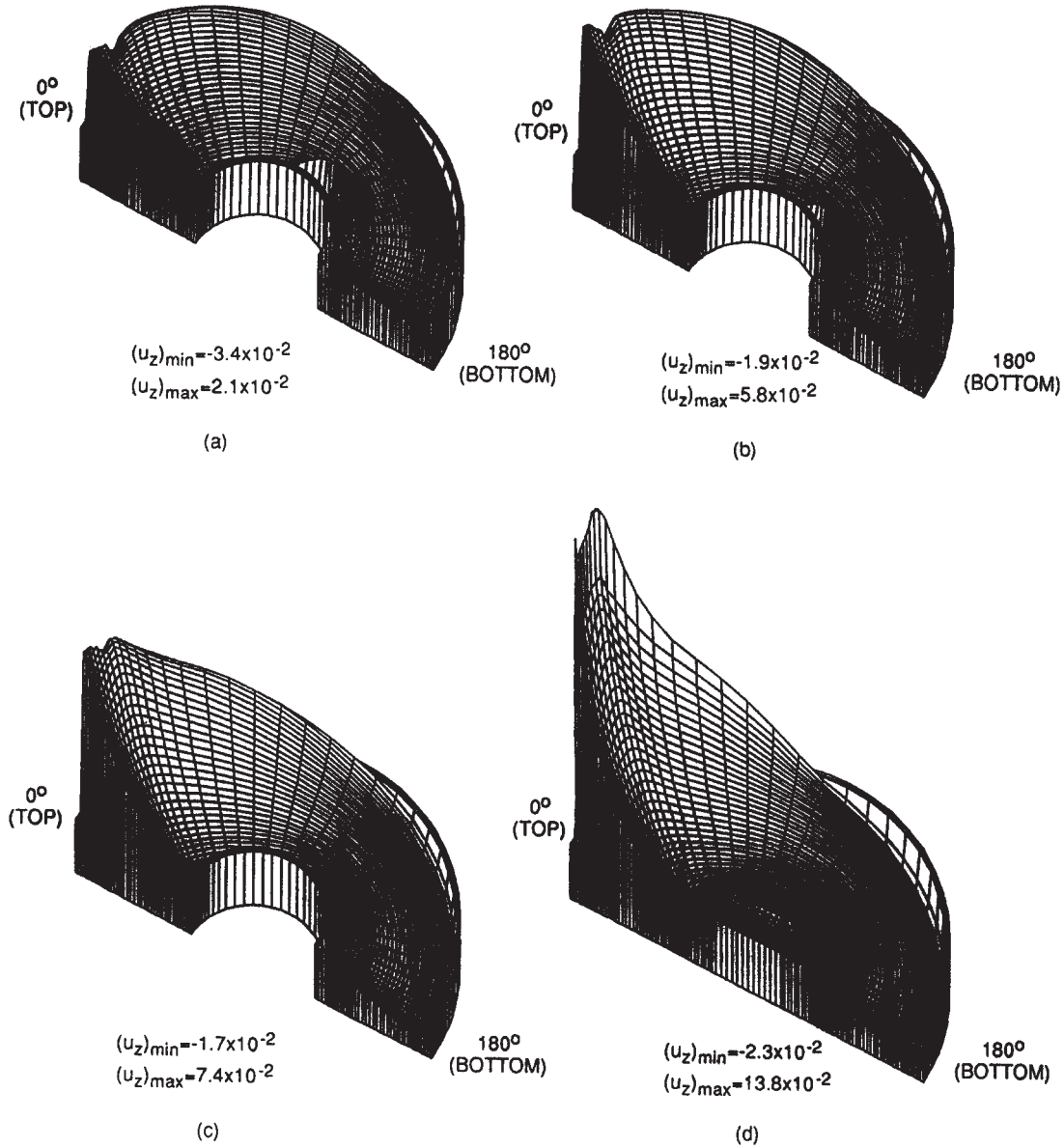
Fig. 5. Axial velocity distribution in different planes of the cavity; $Ra^* = 3.71 \times 10^9$, (a) $z = L/4$, (b) $z = L/2$, (c) $z = 3L/4$, (d) $z = L$ (aperture plane).

dimensionalized with respect to the reference length, i.e. the outer cylinder radius R_o. Finally, for the inner cylinder tip, a total of 13 thermocouples were used.

Figures 7 and 8 display the experimental steady-state surface temperatures for the outer cylinder and end-wall, obtained experimentally for three Rayleigh numbers corresponding to different power inputs to the test section. In each case, the $0°$ location denotes the uppermost position of the cavity. The temperature distribution over the outer cylinder and end-wall exhibit the symmetry ($\pm 2\%$) about the vertical plane of the cavity. The surface temperatures increased steadily from the bottom to the top of the cavity due to an increase in the thermal boundary layer thickness. This situation is analogous to the natural convection flow

over a vertical flat plate with an applied constant heat flux, wherein the thermal boundary layer thickness increases continuously along the upward direction as the fluid convects heat from the surface. For the outer cylinder, the temperature values were lower near the open end of the cavity compared to locations near the end-wall due to two reasons: (i) the decreased boundary layer thickness near the open end of the cavity (due to the penetration of cold fluid into the cavity); (ii) heat conduction from the end-wall to the outer cylinder. This difference in temperatures is more pronounced near the bottom angular position ($\theta = 180°$), because the penetration of fluid into the cavity is primarily through the lower half. For the end-wall, at $\theta = 180°$, i.e. in the lower half of the
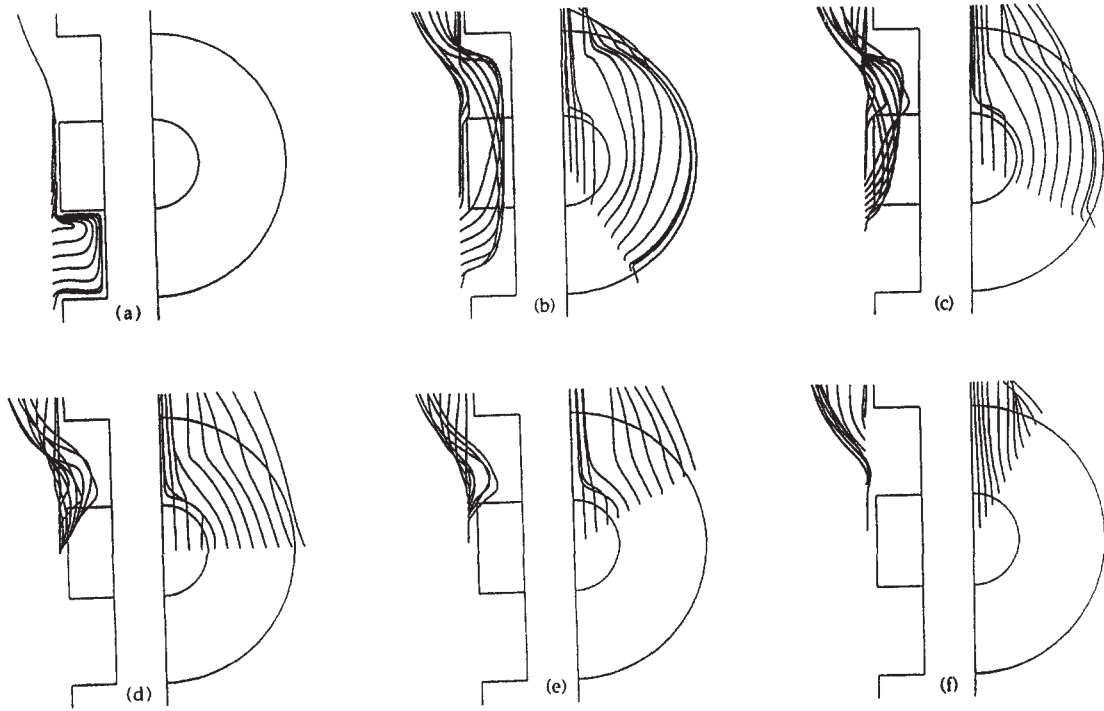
Fig. 6. Particle plots around the cavity $(Ra^* = 3.71 \times 10^9)$, particles introduced at: (a) $\theta = 180^\circ$;
(b) $\theta = 150^\circ$; (c) $\theta = 120^\circ$; (d) $\theta = 90^\circ$; (e) $\theta = 60^\circ$; (f) $\theta = 30^\circ$.

vertical plane, the temperature values are highest for $r = 0.53$ (this thermocouple is located at a greater height than the other two thermocouples). Near the top, this trend reverses, i.e. the temperature values are highest at $r = 0.845$. This is consistent with the analogy drawn earlier with the vertical flat plate boundary layer flow.

The averaged quantities including the mean cavity Nusselt number from the experimental runs for different heating conditions are given in Table 1. In
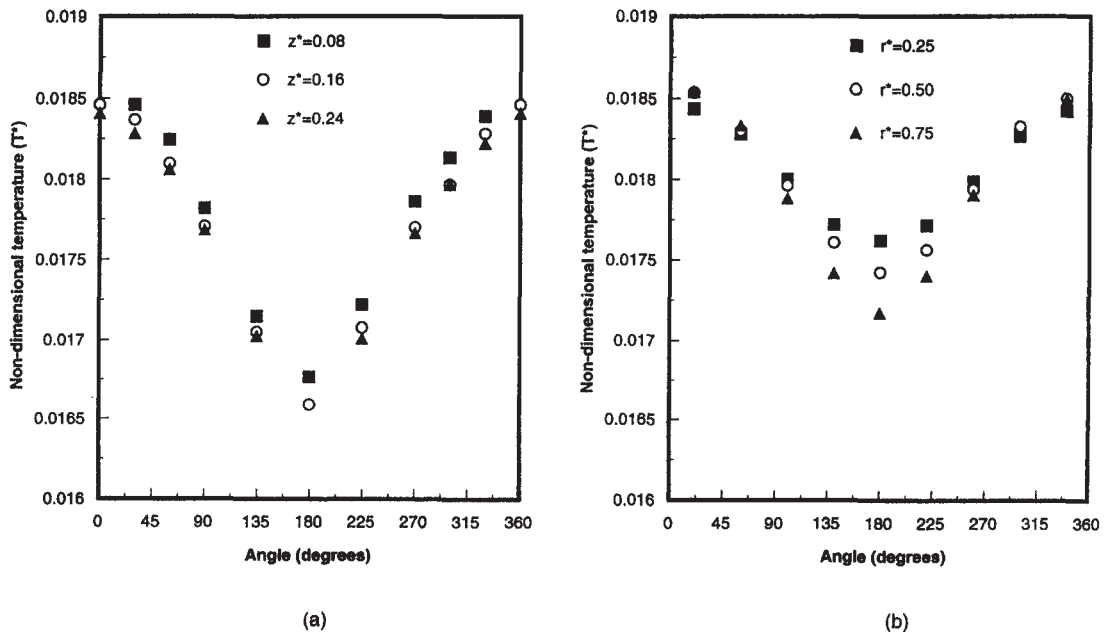
Fig. 7. Experimental temperature distribution for $Ra^* = 3.71 \times 10^9$; (a) outer cylinder, (b) end-wall.
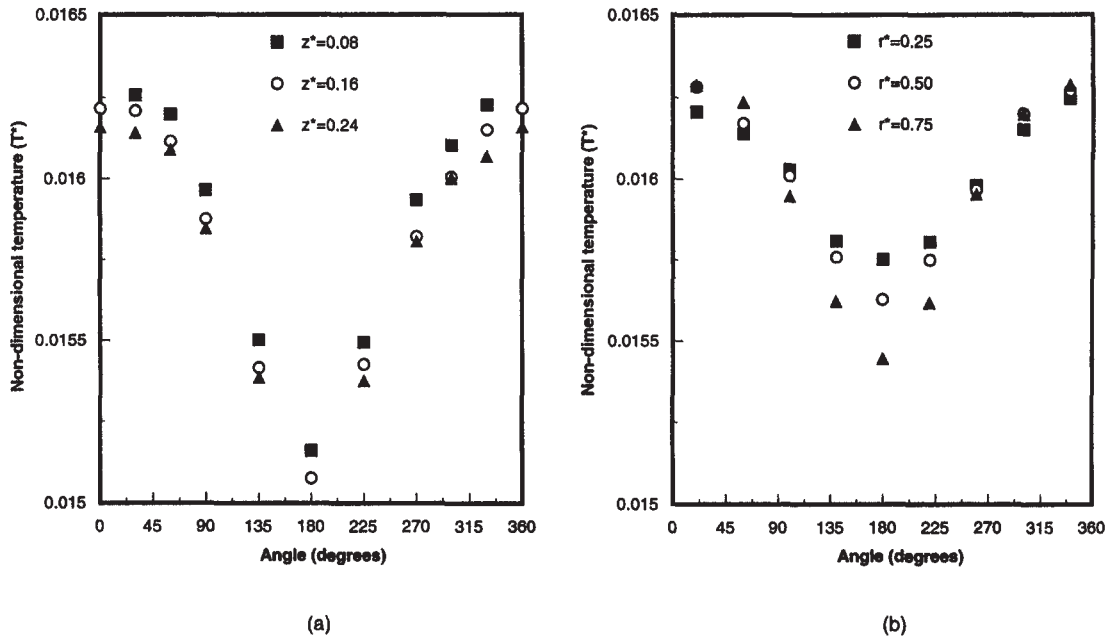
Fig. 8. Experimental temperature distribution for $Ra^* = 5.05 \times 10^9$; (a) outer cylinder, (b) end-wall.

this table, the Nusselt number is a measure of the convective heat transfer rates from each component of the cavity. The cavity Nusselt number provides an estimate of the total convective loss from the annular cavity. The very good agreement between the experimental and numerically predicted heat transfer rates follows directly from the temperature comparisons discussed above, i.e. the agreement is within 12% for the highest Rayleigh number case analyzed numerically. Based on the experimental results, power law correlations for the experimental heat transfer results were obtained as follows:

The mean and maximum deviation of data from the above correlations was 0.5% and 3.3% respectively. Figure 9 shows the isotherms in different planes of the cavity for $Ra^* = 3.71 \times 10^9$. The temperature values in the figure are non-dimensionalized using $(T - T_\infty)/(qR_o/k)$. The temperature distribution shows the presence of sharp gradients around all the cavity surfaces. At the top of the inner cylinder, flow separation leads to the formation of a buoyant plume resulting in a drastic reduction in the temperature gradients around that location. For the outer cylinder, it can be seen that the thermal boundary layer thickness increases

Outer cylinder: $Nu_{av} = 0.0136(Ra^*)^{0.376}$
End-wall: $Nu_{av} = 0.0133(Ra^*)^{0.379}$
Inner cylinder: $Nu_{av} = 0.0113(Ra^*)^{0.381}$ for $1.27 \times 10^9 < Ra^* < 5.05 \times 10^9$.
Inner cylinder tip: $Nu_{av} = 0.0119(Ra^*)^{0.378}$
Cavity: $Nu_{av} = 0.0131(Ra^*)^{0.378}$

Table 1. Experimental mean heat transfer results

| Ra^*	Pr	Mean temperature (non-dimensional)					Nu_{av} (cavity)
		Outer cylinder	End-wall	Inner cylinder	Inner cylinder tip	Cavity	
1.27×10^9	0.721	2.579×10^{-2}	2.620×10^{-2}	2.617×10^{-2}	2.584×10^{-2}	2.603×10^{-2}	36.72
2.73×10^9	0.702	2.014×10^{-2}	2.041×10^{-2}	2.043×10^{-2}	2.014×10^{-2}	2.017×10^{-2}	47.08
3.71×10^9	0.700	1.772×10^{-2}	1.799×10^{-2}	1.806×10^{-2}	1.781×10^{-2}	1.789×10^{-2}	53.41
4.48×10^9	0.698	1.684×10^{-2}	1.703×10^{-2}	1.701×10^{-2}	1.681×10^{-2}	1.694×10^{-2}	56.41
5.05×10^9	0.697	1.582×10^{-2}	1.599×10^{-2}	1.589×10^{-2}	1.574×10^{-2}	1.589×10^{-2}	60.12
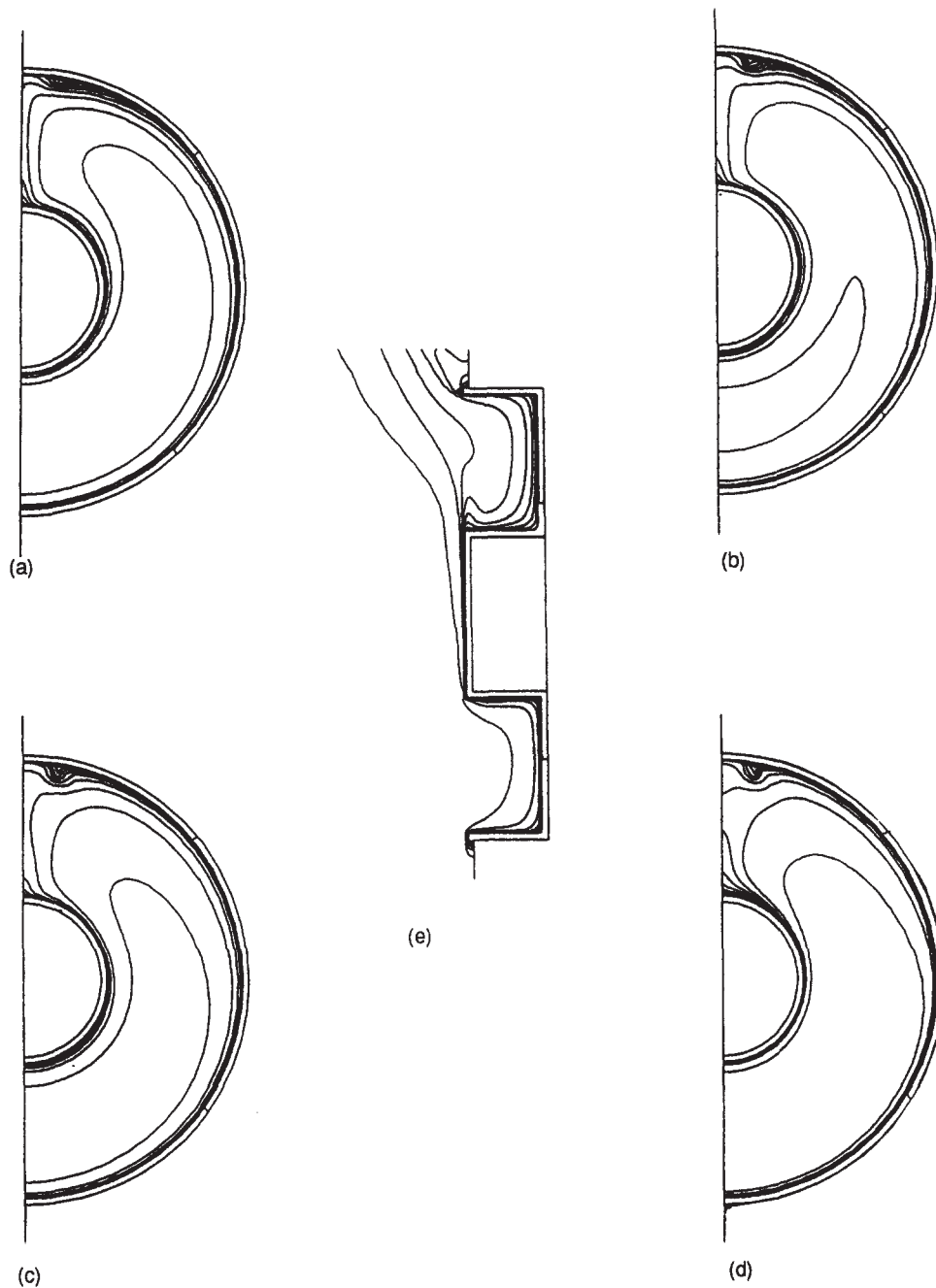
Fig. 9. Isotherms in different planes of the cavity; $Ra^* = 3.71 \times 10^9$ (range: 10^{-3}–1.9×10^{-2}, $\Delta T = 2 \times 10^{-3}$).
(a) $z = L/4$, (b) $z = L/2$, (c) $z = 3L/4$, (d) $z = L$ (aperture plane), (e) symmetry plane.

steadily from bottom to top, indicating higher heat transfer rates in the lower half of the cavity. As the plume rising from the inner cylinder negotiates the curved surface of the outer cylinder, it encounters the upward flow along the outer cylinder resulting in a stagnant zone about 5–10° from the top. This causes the slight distortion of isotherms in the corresponding location near the outer cylinder. The distortion was observed to be more pronounced near the open end

of the cavity, due to the reduced resistance to the buoyant flow.

A comparison between the numerical and experimental results is shown in Fig. 10. The local temperature distribution over the outer cylinder, end-wall and the inner cylinder is compared for the heating condition corresponding to $Ra^* = 3.71 \times 10^9$. Considering the complexity of the physical phenomena involved in the open annular cavity natural convection
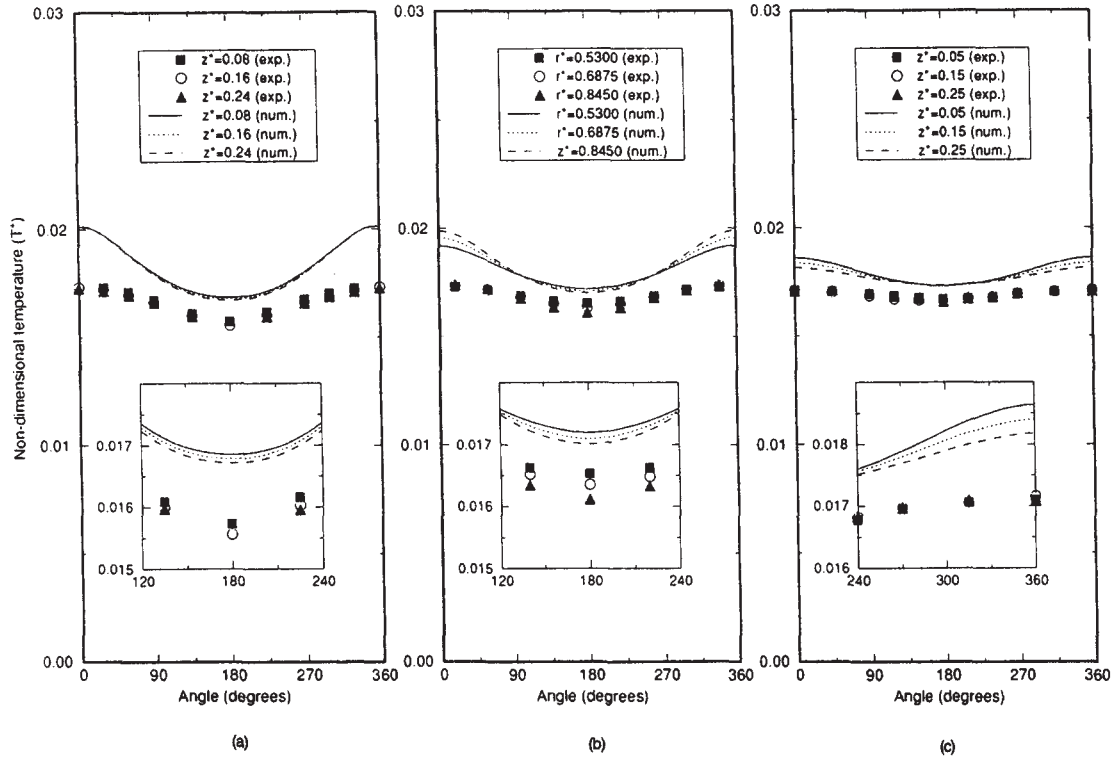
Fig. 10. Comparison of experimental and numerical surface temperatures; $Ra^* = 3.71 \times 10^9$, (a) outer cylinder, (b) end-wall, (c) inner cylinder.

flow, the very good agreement can be seen between the experimental and numerical results. Upon closer examination of the temperature values from the numerical and experimental results, it was observed that they display precisely the same trend at different axial and radial locations. Additional computations were carried out for $Ra^* = 1.27 \times 10^9$ and 5.05×10^9. A comparison between the experimental and numerically predicted mean component temperatures under different heating conditions is shown in Table 2. Similar trends were obtained from a comparison of the experimental and numerical Nusselt numbers.

5. CONCLUSIONS

Fluid flow and heat transfer characteristics of natural convection around an open annular cavity have been investigated. The results presented in this paper provide foremost experimental data pertaining to buoyancy-induced flows in open ended annular cavities. This data can be used to validate numerical algorithms for this category of flows, as was done in the present work. Heat transfer correlations have been obtained experimentally to predict the heat losses from the cavity.

Table 2. Comparison between experimental and numerical results

| Ra^* | Method | Mean temperature (non-dimensional) | | | | |
		Outer cylinder	End-wall	Inner cylinder	Inner cylinder tip	Cavity
1.27×10^9	Experimental	2.579×10^{-2}	2.620×10^{-2}	2.617×10^{-2}	2.584×10^{-2}	2.603×10^{-2}
	Numerical	2.593×10^{-2}	2.593×10^{-2}	2.582×10^{-2}	2.582×10^{-2}	2.593×10^{-2}
	% difference	$+0.2$	-0.61	-0.61	0.0	-0.2
3.71×10^9	Experimental	1.772×10^{-2}	1.799×10^{-2}	1.806×10^{-2}	1.781×10^{-2}	1.789×10^{-2}
	Numerical	1.907×10^{-2}	1.919×10^{-2}	1.888×10^{-2}	1.868×10^{-2}	1.907×10^{-2}
	% difference	$+5.72$	$+5.00$	$+3.47$	$+3.61$	$+4.91$
5.05×10^9	Experimental	1.582×10^{-2}	1.599×10^{-2}	1.589×10^{-2}	1.574×10^{-2}	1.589×10^{-2}
	Numerical	1.796×10^{-2}	1.806×10^{-2}	1.777×10^{-2}	1.761×10^{-2}	1.796×10^{-2}
	% difference	$+11.2$	$+10.7$	$+9.75$	$+9.75$	$+10.7$

The experimental data has been verified by comparison against results obtained from a finite element analysis of the problem. The results provided an in-depth understanding of the basic mechanisms underlying the buoyancy induced flow in open ended cavities. The flow field results indicate the strong influence of the open end on the flow field within the cavity. The bulk flow is characterized by the suction of cold fluid into the lower portions of the cavity and ejection of hot fluid as a buoyant jet from the top of the cavity. This interaction between the inner and outer flow fields is responsible for enhanced heat transfer rates from open ended cavities.

REFERENCES

1. P. Le Quere, J. A. C. Humphrey and F. S. Sherman, Numerical calculation of thermally driven two-dimensional unsteady laminar flow in cavities of rectangular cross section, *Numer. Heat Transfer* **4**, 249–283 (1981).
2. P. Penot, Numerical calculation of two-dimensional natural convection in isothermal open cavities, *Numer. Heat Transfer* **5**, 421–437 (1982).
3. Y. L. Chan and C. L. Tien, A numerical study of two-dimensional natural convection in square open cavities, *Numer. Heat Transfer* **8**, 65–80 (1985).
4. J. A. C. Humphrey and W. M. To, Numerical simulation of buoyant turbulent flow—II. Free and mixed convection in a heated cavity, *Int. J. Heat Mass Transfer* **29**, 593–610 (1986).
5. K. Vafai and J. Ettefagh, The effects of sharp corners on buoyancy driven flows with particular emphasis on outer boundaries, *Int. J. Heat Mass Transfer* **33**, 2311–2328 (1990).
6. K. Vafai and J. Ettefagh, Thermal and fluid flow instabilities in buoyancy-driven flows in open ended cavities, *Int. J. Heat Mass Transfer* **33**, 2329–2344 (1990).
7. A. Bejan and S. Kimura, Penetration of free convection into a lateral cavity, *J. Fluid Mech.* **103**, 465–478 (1981).
8. V. Sernas and I. Kyriakides, Natural convection in an open cavity, *Proc. 7th Int. Heat Transfer Conf., Munich, Germany*, Vol. 2, pp. 275–286 (1982).
9. C. F. Hess and R. H. Henze, Experimental investigation of natural convection losses from open cavities, *ASME J. Heat Transfer* **106**, 333–338 (1984).
10. Y. L. Chan and C. L. Tien, Laminar natural convection in shallow open cavities, *ASME J. Heat Transfer* **108**, 305–309 (1986).
11. K. Vafai and J. Ettefagh, Axial transport on natural convection inside of an open ended annulus, *ASME J. Heat Transfer* **113**, 627–634 (1991).
12. C. Desai and K. Vafai, Three-dimensional buoyancy-induced flow and heat transfer around the wheel outboard of an aircraft, *Int. J. Heat Fluid Flow* **13**, 50–64 (1992).
13. S. J. Kline and F. A. McClintock, Describing uncertainties in single sample experiments, *Mech. Engng* **January**, 3–8 (1953).
14. R. J. Moffat, Describing the uncertainties in experimental results, *Exp. Therm. Fluid Sci.* **1**, 3–17 (1988).
15. V. Haroutunian and M. S. Engelman, On modeling wall-bound turbulent flows using specialized near-wall finite elements, *Adv. Numer. Sim. Turbulent Flows, ASME-FED* **117**, 97–105 (1991).
16. C. P. Desai and K. Vafai, An investigation and comparative analysis of two-dimensional and three-dimensional turbulent natural convection in a horizontal annulus, *Int. J. Heat Mass Transfer* **37**, 2475–2504 (1994).
17. Y. L. Chan and C. L. Tien, A numerical study of two-dimensional laminar natural convection in shallow open cavities, *Int. J. Heat Mass Transfer* **28**, 603–612 (1985).
18. FIDAP Theoretical Manual, *Fluid Dynamics International*. Evanston, IL (1993).
19. T. H. Kuehn and R. J. Goldstein, An experimental and theoretical study of natural convection in the annulus between horizontal concentric cylinders, *J. Fluid Mech.* **74**, 695–719 (1976).
20. K. Fukuda, Y. Miki, N. Taniguchi, K. Morita and S. Hasegawa, Direct simulation and large eddy simulation of turbulent natural convection in a horizontal annulus, *Mem. Fac. Engng Kyushu Univ.* **51**, 355–369 (1991).
21. A. E. McLeod and E. H. Bishop, Turbulent natural convection of gases in horizontal cylindrical annuli at cryogenic temperatures, *Int. J. Heat Mass Transfer* **32**, 1967–1978 (1989).